ELIMINATION OF SURFACE TENSION EFFECT ON A SMALL PLATE BY

DEVELOPING SUPERWETTING SURFACES

by

VARUN GARG

Presented to the Faculty of the Graduate School of

The University of Texas at Arlington in Partial Fulfillment

of the Requirements

for the Degree of

Master of Science in Mechanical Engineering

THE UNIVERSITY OF TEXAS AT ARLINGTON

August 2014

Acknowledgements

In my past two years as a graduate student at the University of Texas at Arlington, I have been fortunate enough to know several people without their valuable help and input this thesis would not have been possible. It gives me great pleasure to express my gratitude towards them.

Foremost, I express my sincere thanks to my advisor, Dr. Cheng Luo for his valuable guidance, advice and encouragement throughout the course of my research. I have benefited immensely from Dr. Luo's mentorship and knowledge. For that, I am forever indebted to him.

I would like to thank Dr. Hyejin Moon and Dr. Dennis DeSheng Meng for taking time to serve on my thesis committee and for their valuable suggestions and comments.

I gratefully thank Dr. Lei Qiao for mentoring me throughout my research and who patiently trained me on various fabrication processes, techniques and experimentation setup. This thesis work was not possible without his help.

I would like to thank Mingming Xiang and Xin Heng for their valuable discussions and help in the lab on countless occasions. I really appreciate their professionalism and I have learnt a lot from their work ethics.

I would like to thank the staff at the Nanofab research centre and CCMB at UTA for training me on various instruments. My thanks to Dr. Nader Hozhabri, Dennis Bueno, Richard K. Chambers and Richard E. Wells at Nanofab and Dr. Dr. Jiechao Jiang and David Yan at CCMB for making life smooth and pleasant at these facilities.

I would like to thank Debi Barton, Lanie Gordon, Louella Carpenter and the entire staff at the Mechanical and Aerospace department at UTA for their constant help and support.

Abstract

ELIMINATION OF SURFACE TENSION EFFECT ON A SMALL PLATE BY

DEVELOPING SUPERWETTING SURFACES


Varun Garg, MS

The University of Texas at Arlington, 2014

Supervising Professor: Cheng Luo

In this work, we explored the possibility of creating superwetting surfaces, which are defined here as the ones with apparent contact angles less than $5^o$, using roughness structures for the purpose of eliminating surface tension effect on a floating small plate. It is often considered that the ratio of the actual roughness surface over the projected one plays a critical role in generating superwetting surfaces. However, we found that the ratio of the top surfaces of roughness structures over the projected one had more influence on apparent contact angles. As this ratio was less than 0.013, the resulting apparent contact angle might be less than $5^o$, when the intrinsic contact angle was $40^o$ or above. Accordingly, hybrid micro/nanostructures, which had such a small ratio, were chosen to create the superwetting surfaces. These surfaces were subsequently applied to eliminate surface tension effect on a small plate. As a result of this elimination, the small plate that was denser than the liquid sank down to the liquid bottom.

Table of Contents

List of Illustrations

List of Tables

Chapter 1

Introduction

Surface tension is an effect within the surface of the liquid which acts tangentially to the interface between liquid and the floating object, pointing out of this object. Although some small objects such as water striders [1, 2], sewing needles, water strider robots [3], mm-scaled boats [4-6], cm-scaled gels [7], flotillas [8] and boats [9] are denser than water, surface tension allows them to float on the surface of water. On the other hand, take small submarines and water robots as examples. They may need to both stay under liquid and float on liquid surfaces for different applications, as in the case of a large-scale submarine. Therefore, a question arises: is it possible to find a simple approach to eliminate surface tension such that a small object can easily sink down to the liquid bottom, while the effect of the surface tension can also be retained, if needed, for the small object to float on the liquid surface? To answer this question, we develop such an approach in this work by covering one side of a small object with specifically designed roughness structures.

In the past two decades, a lot of work has been done on studying surfaces with lyophobic properties with contact angles larger than 90°. Superhydrophobic (contact angles are larger than 150$^{o}$) structures can be created by the manipulation of surface roughness and texture which has been inspired from biological materials. It is observed that some so-called "self-clean" plants, such as Lotus and Colocasia, can form spherical (superhydrophobic) water droplets on their leaves in rain, fog and dew to avoid getting wet (Figure 1-1). This phenomenon is often called "Lotus effect" [10].It was found that the roughness structures on the leaves took a great role in this effect [10, 11]. Accordingly, lyophobic structures have been widely applied to enhance surface lyophobicity. In a

recent work, we have also shown that micropillars can be applied to trap air under water, thus increasing buoyancy of a small plate [12].

Superwetting surfaces refer to one on which liquid spreads to nearly zero contact angle. Lyophilic structures can be employed to enhance surface lyophilicity [13, 14].In this work, we explore the possibility of applying lyophilic structures to eliminate surface tension effect on a small plate.

(a)                                (b)
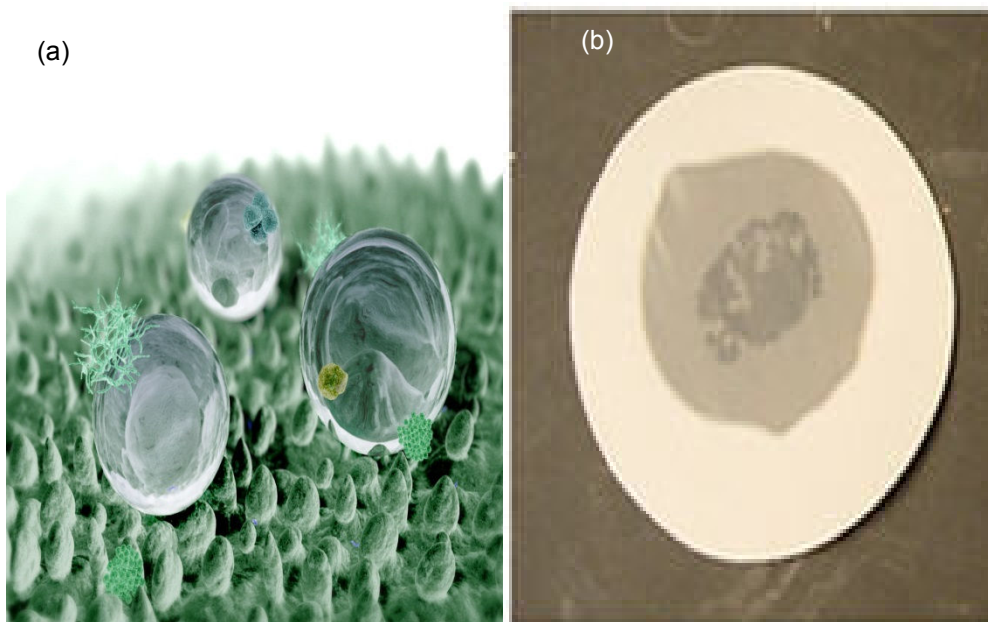


Figure 1-1: (a) Liquid drop on a superhydrophobic lotus leaf. [Image source: www.wikipedia.com]. (b) Superlyophilic surface. [Image source: www.millipore.com].

1.1 Wetting Theory

*1.1.1 Contact Angle*

In the study of wetting phenomena, an important parameter used to quantify the extent of wetting is the contact angle. The theoretical description of contact angle arises from the consideration of thermodynamic equilibrium between the three phase system with a solid surface, a fluid and a vapor. The line along the solid surface where all three phases meet is the contact line. The contact angle is therefore defined as the angle measured through the liquid, where a liquid/vapor interface meets a solid surface as shown in Figure 1-2.
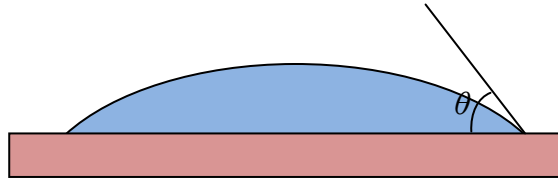


Figure 1-2: Schematic diagram showing contact angle of a liquid drop on a surface.

*1.1.2 Wetting States*

a)  Wenzel state: In this wetting state (Figure 1-3), the drop completely fills roughness grooves. The corresponding apparent contact angle is defined by the following equation [15]:

$$\cos\theta_a = r\cos\theta_c,$$

(1-1)

where *r* denotes the roughness factor, equal to the ratio of the solid surface area to its flat projected area, $\theta_a$ denotes apparent contact angle and $\theta_c$ denotes intrinsic contact angle. According to this equation, if the contact

3

angle on the smooth surface (i.e., intrinsic contact angle) is larger than 90°, roughness will further increase the observed contact angle (i.e., apparent contact angle).Otherwise, roughness will reduce the apparent contact angle.
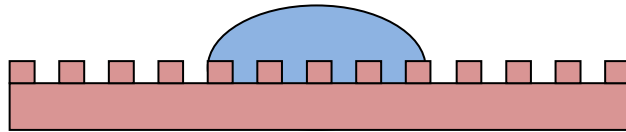


Figure 1-3: Schematic diagram showing wetting in Wenzel state on rough surface.

b) Cassie-Baxter state: In this wetting state, the droplet sits on a composite air-solid surface (Figure 1-4). The corresponding apparent contact angle is defined by the following equation [16]:

$$\cos\theta_a = rf\cos\theta_c + f - 1,$$

(1-2)

where $f$ denotes the ratio of the top surface of roughness structures over the projected one. According to this equation, if intrinsic contact angle larger than 90°, roughness will further increase apparent contact angle. This equation may not be valid when the intrinsic contact angle is less than 90°, since a liquid may completely penetrate the roughness structures, changing the wetting state to another one.
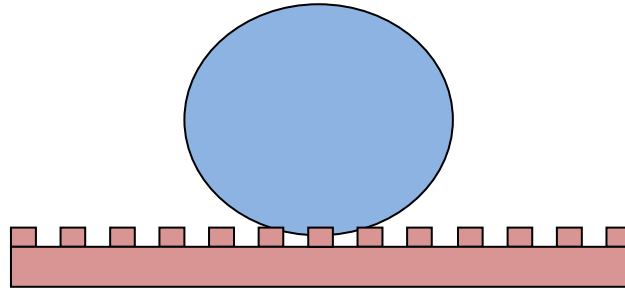
Figure 1-4: Schematic diagram showing wetting in Cassie Baxter state on rough surface.

c) Cassie Impregnating state: In this wetting state, the roughness structures may guide the liquid causing the liquid front to move away from the droplet in the form of a thin precursor film (Figure 1-5). This phenomenon which is in between of spreading and imbibition is also known as hemi-wicking. In such a state, the equilibrium contact angle is given by [17,18]:

$$\cos\theta_a = f\cos\theta_c + (1-f).$$
(1-3)
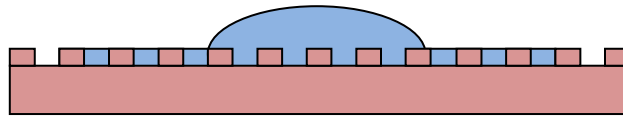


Figure 1-5: Schematic diagram showing wetting in Cassie impregnating state on rough surface.

*1.1.3 Capillary Effect*

Capillary action is the ability of the liquid to flow in narrow spaces without the assistance of, and in opposition to, external forces like gravity (Figure 1-6). It occurs due to the pressure of cohesion and adhesion which causes the liquid to work against the gravity. There exists a particular length referred to as capillary length beyond which effect of gravity becomes important. It is estimated by comparing Laplace pressure to hydrostatic pressure. Capillary length $K^{-1}$ is given by:

$$K^{-1} = \sqrt{\frac{\gamma}{\rho g}}$$
.
(1-4)

where $\gamma$ is the surface tension of the fluid-fluid interface, $\rho$ is the fluid density and $g$ is the acceleration due to gravity. Capillary length for water is 2.7 mm.
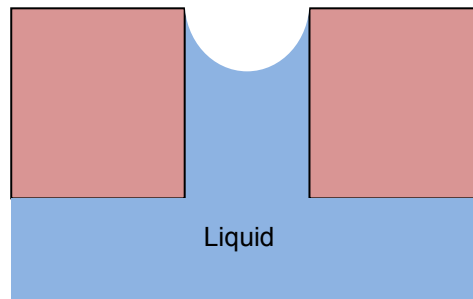


Liquid

Figure 1-6: An illustration of liquid rising due to capillary effect.

*1.1.4 Young-Laplace Equation*

This equation relates a difference of pressure across an interface to the curvature of the interface. This force is direct result of surface tension, since a greater curvature leads directly to a greater imbalance between the internal and external energy of the surface molecules. This equation gives the relation between the size of the liquid meniscus and the Laplace pressure. The Young-Laplace equation is given by:

$$p_w - p_a = \gamma \left( \frac{1}{R_1} + \frac{1}{R_2} \right),$$

(1-5)

where $\gamma$ represents the surface tension of the liquid, $R_1$ and $R_2$ are radii of the maximal and minimal curvatures at some point on the liquid surface and ($p_w$ - $p_a$) is the so called Laplace pressure.

## 1.2 The Effect of Surface Tension at Micro Scale

The behavior of liquids at a microscopic scale is different from that for liquids at macroscopic level. At macroscopic level, the pressure is well above or below atmospheric pressure and gravity dominates fluid dynamics, while surface tension and capillary forces are generally negligible. On the other hand at microscopic scale, the pressure range in microfluidic system is generally well below the atmospheric pressure, and gravitational effects are minimal due to the exceedingly small volumes employed. As volume decreases, the surface to volume ratio increases, hence it is not surprising that surface tension and capillary effect closely related to each other, dominate the fluid mechanics at microscopic scale. There exists an interfacial tension referred as surface tension at the interfacial surface. Molecules or atoms in a bulk medium attract one another through Van der Waals forces or dipole interactions for polar molecules. Molecules at an interface

7

experience an uneven force since the attractive force for the second medium will likely be different than that of the first. Therefore this difference in the cohesive energy pulling a molecule into or out from the bulk medium is represented by surface tension which takes the units of N/m, suggesting the behavior of surface tension as a force.

Chapter 2

Theoretical Model

Consider a small rectangular plate having vertical sidewalls, which is denser than the surrounding liquid (Figure 2-1). The length, width and height are represented by $a$, $b$ and $c$, respectively. When this plate is put on the liquid surface, a curved air/liquid interface is formed beside the plate. This surface extends from the original liquid surface to the top of the solid fragment. As illustrated in Figure 2-2, let $AB$ denote part of the air/liquid interface, where $A$ represents the three phase (air/liquid/solid) contact line located at the plate and $B$ represents the intersection of the air/liquid interface with the original liquid surface. Accordingly $AB$ is below the original liquid surface [19]. Let $F_S$ denote total supporting force which is the vertical resultant of air pressure, liquid pressure and surface tension induced force. This force is: [19]

$$F_s = \rho_l g (V_1 + V_2 + V_3),  \tag{2-1}$$

where $\rho_l$ denotes mass density of the liquid, and $g$ is the acceleration due to gravity. $V_1$, $V_2$ and $V_3$ respectively are the volume of the small plate, volume of the region enclosed by vertical surfaces and volume formed by the air/liquid profile, the original liquid surface and the vertical surface. Set

$$V = V_1 + V_2 + V_3,  \tag{2-2}$$

where $V$ is the actual volume of the liquid displaced due to the floating of the small plate on the liquid surface. Thus, $F_s$ is equal to the total weight of the liquid displaced, and is the buoyancy that the small plate has.
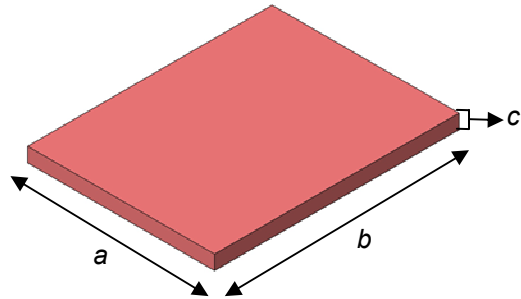
Figure 2-1: An illustration of a small plate.

Let *G* be the total weight of the small plate which equals:

$$G = \rho_s g V_1,$$

<div align="right">(2-3)</div>

where $\rho_s$ represents the mass density of small plate. *G* can be re written as

$$G = \rho_s g a b c.$$

<div align="right">(2-4)</div>
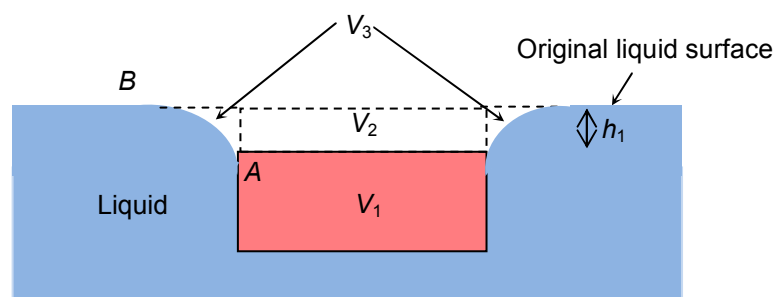


Figure 2-2: Side view of a small plate floating on liquid surface.
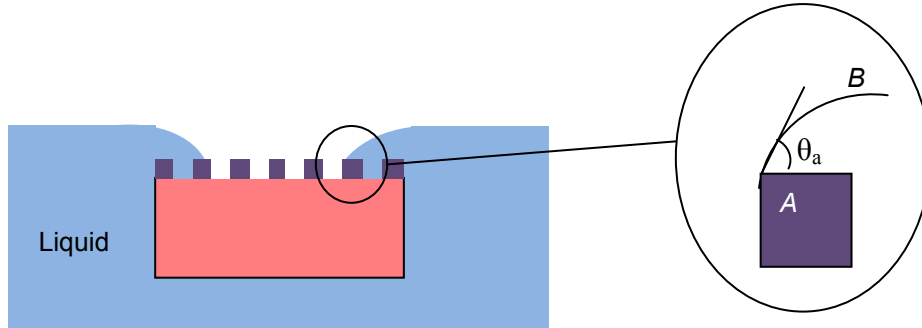
Figure 2-3: Side view of a floating small plate with the cross sectional view of the air/liquid interface showing the apparent contact angle ($\theta_a$).

As shown in Figure 2-2, $V_2 = abh_1$. Also considering force balance on the air/liquid interface. On the original liquid surface, $\gamma$ is along the horizontal direction. Let $h$ denote the vertical distance between the original liquid surface and liquid pressure at a point on the air/liquid interface. The air and liquid pressure at this point are $p_o$ and ($p_o$ + $\rho gh$) respectively. Thus the vertical force generated by the air and liquid pressure is equal to $\rho gV_3$, where $V_3$ is the volume formed by the air/liquid profile, the original liquid surface and the vertical surface. After balancing the forces in the vertical direction, according to [19], we have:

$$2\gamma \sin \theta_a (a + b) = \rho_l g V_3,$$

(2-5)

where $\theta_a$ is the advancing apparent contact angle on the plate. Set $\theta_c$ be the intrinsic contact angle of liquid on the plate. In our case both the angles are assumed to be less than 90°. According to [19], the maximum value of $F_s$ is

$$F_{s\max} = \rho_l gabc + 2ab\sqrt{\rho_l g\gamma} \sin \frac{\theta_a}{2} + 2\gamma(a + b)\sin \theta_a,$$

(2-6)

where the three terms on the right hand side are the mathematical expressions of $\rho g V_1$, $\rho g V_2$ and $\rho g V_3$, respectively. It can be observed from this equation that the second and third terms on right hand side are both surface tension related forces, Also $F_s$ can be simplified by comparing the critical dimensions of the solid fragment with capillary length of the liquid. Let's assume the capillary length of water be 2.73 mm for instance, If the critical dimensions are much larger than 2.73 mm, then the two surface tension related forces become negligible in comparison with $\rho gabc$. Hence the buoyancy of a large scale object is considered to be $\rho gabc$. On the other hand, when the critical dimensions of the solid fragment are neither much large nor smaller than 2.73 mm, all three forces may have significant contribution to the buoyancy. In this case, our motive is to eliminate the surface tension effect, accordingly if by surface treatment $\theta_a$ becomes nearly 0°, then $F_{smax}$ is approximately $\rho_l gabc$ thus $V_2$ and $V_3$ are nearly reduced to zero. We also know that $\rho_s > \rho_l$, $F_{smax} < G$. which will eliminate the surface tension effect and the small plate should sink. On the other hand, when the small plate is flipped over with the untreated surface facing up, it will not sink, implying that the surface tension effect still exists.

Hence in order to sink the small plate, we have to treat the surface of the small plate in such a way that $\theta_a$ becomes nearly 0, eliminating surface tension effect. This can be done either by introducing a coating whose advancing intrinsic contact angle is 0° or by introducing roughness structures. In this work we will focus on creating the lyophilic roughness structures. As described in chapter 1, two wetting states exist when the liquid comes in contact with lyophilic structures: Wenzel and Cassie impregnating [17, 18]. Cassie impregnating state is similar to that of Wenzel state, while it includes a thin film of liquid which fills the textured surfaces around the liquid drop. We will consider the possibility of creating very small $\theta_a$ in these two wetting states in the following sub sections.

## 2.1 Using Wenzel State to Create Small $\theta_a$

In this sub section we will consider the possibility of creating small apparent angle using the Wenzel equation. Wenzel state can predict the enhancement of wetting which uses the roughness ratio and the intrinsic contact angle to predict the apparent contact angle. $\theta_a$ is related to $\theta_c$ by [15]

$$cos\theta_a = rcos\theta_c, \tag{2-7}$$

where $r$ denotes the ratio of the total area of the rough surface to the projected or planar area. $r$ is always larger than 1 to denote a rough surface. When $r$ is 1, it implies that the surface is smooth. In our case we have

$$r \geq 1. \tag{2-8}$$

The Wenzel equation indicates that when the intrinsic contact angle $\theta_c < 90°$, the apparent contact angle $\theta_a$ will decrease with the increase in $r$ provided that $\theta_c$ also decrease. When the Wenzel equation applies, the solid remains dry beyond the drop when the surface composition is given by

$$\theta_c > \theta_1, \tag{2-9}$$

where $\theta_1$ is the critical angle, and according to [17], it is given by:

$$\cos\theta_1 = \frac{1-f}{r-f}, \tag{2-10}$$

where $f$ denotes the ratio of the top surfaces of the roughness structures to the projected area. We have

$$0 < f \leq 1. \tag{2-11}$$

When $f$ is 1, it also implies that the surface is smooth. Thus we have $r > 1$ and $f < 1$ so that condition 2-10 defines a critical contact angle intermediate between 0 and $\pi/2$.

According to a condition derived by Concus and Finn [20-22], a liquid loses its stability and propagates along the corners of the roughness structures, when its intrinsic contact angle $\theta_c$ is smaller than 45°. But in the case of Wenzel state, propagation of liquid along the corners of roughness structures does not occur as the solid remains dry beyond the drop. Thus $\theta_c$ has to be larger than 45°, and according to the inequality 2-9,

$$\theta_1 \geqslant 45^\circ.$$
(2-12)

$\theta_1$ follows an increasing trend if $r$ and $f$ are increased as observed form Eq. 2-10. To satisfy the inequality 2-12, $r$ has to be equal to or greater than $\sqrt{2}$. Otherwise inequality 2-12 is violated. $\theta_1$ is calculated by using Eq. 2-10 if $r$ is greater than or equal to $\sqrt{2}$. $\theta_1$ is equal to 45° when $r$ is less than $\sqrt{2}$.

We will now consider the possibility of creating small $\theta_a$ in Wenzel state by considering the following cases:

1. Using Eq. 2-7, we will try to predict if $\theta_a$ can become near $0^0$. For example, let us consider $\theta_c$ to be 35°, and $r$ close to 1.5, which can be achieved by fabricating roughness structures on the surface of the solid fragment. We observe that $\theta_a$ is decreasing and approaching 0°. However, as $\theta_c$ is less than 45°, Inequality 2-9 is not met and the wetting is not in Wenzel state. Hence Eq. 2-7 is not valid in this case and $\theta_a$ may not be close to 0°.

2. In this case we will consider the lower limit of the apparent contact angle, i.e. the minimum value of $\theta_a$ when the intrinsic contact angle, $\theta_c$ is approaching its lower limit which is $\theta_1$ according to Eq. 2-7 and Eq. 2-10, we have

$$\cos\theta_{a\min} = \frac{r(1-f)}{r-f},$$
(2-13)

where $\theta_{amin}$ denotes the lower limit of $\theta_a$. The values of $\theta_1$ and $\theta_{amin}$ are calculated using Eq. 2-10 and Eq. 2-13 respectively, which is given in Figure 2-4 when $f$ is ranging from 0.1 to 1 with an increment of 0.1. Figure 2-5 shows the results when $f$ varies from 0.0005 to 0.0095 with an increment of 0.001. In both the figures, to satisfy Ineq. 2-12, three values of $r$ are chosen which are $\sqrt{2}$, 5 and 10, to show the range of the values of $\theta_1$ and $\theta_{amin}$. We can observe the following three points from the two figures:

i.    Increasing the roughness factor $r$ does not necessarily result in a small $\theta_a$, as observed from Eq. 2-13 and 2-10, both $\theta_1$ and $\theta_{amin}$ increase with increase in $r$ and $f$. For example when $f$ is fixed to 0.5 and $r$ is increased from $\sqrt{2}$ to 10, $\theta_{amin}$ increases from 35° to 60°. Meanwhile $\theta_1$ changes from 45° to 85°.

ii.    To make $\theta_{amin}$ less than 5°, $f$ should be less than 0.01 and 0.005, for $r = \sqrt{2}$ and 10 respectively.

iii.    For a given $\theta_c$, $r$ may be chosen with aid of Eq. 2-10 to satisfy Ineq.2-9.

## 2.2 Using Cassie Impregnating State to Create Small $\theta_a$

In this case, a film develops in the texture with the penetration front moving away from the drop where $\theta_a$ is related to $\theta_c$ by

$$\cos\theta_a = f\cos\theta_c + (1 - f).$$

(2-14)

Where $f$ denotes the ratio of the top surfaces of the roughness structures over the projected one. It is observed from the above equation that $\theta_a$ increases with the increase in both $f$ and $\theta_c$. Hence in order to get a small $\theta_a$ for a given $\theta_c$, $f$ has to be very less.  If

the intrinsic contact angle is less than the critical contact angle, a film of liquid develops in the texture and the drop sits upon a mixture of solid and liquid. Hence we should have,

$$\theta_c < \theta_1. \tag{2-15}$$

In order to estimate the maximum value of $\theta_a$ in this wetting state, $\theta_c$ should approach its upper limit, which is $\theta_1$. By substituting Eq. 2-10 in Eq. 2-14, we get

$$\cos\theta_{a\max} = \frac{r(1-f)}{r-f}, \tag{2-16}$$

where $\theta_{a\max}$ denotes the upper limit of $\theta_a$. It is interesting to see by comparing Eq. 2-16 and 2-13 the right hand side of both the equations are same. This has the following two implications

i. The $\theta_{a\min}$-$f$ curves in Figure 2-4 and Figure 2-5 for the Wenzel state are actually the ones of $\theta_{a\max}$-$f$ in the Cassie impregnating state. Figure 2-4 and Figure 2-5 give $\theta_{a\max}$ that corresponds to that $\theta_c = \theta_1$.

ii. In comparison with Wenzel state, Cassie impregnating has a smaller $\theta_a$ for given values of $f$ and $r$. i.e. having the same surface texture.

For a given $\theta_1$, when $\theta_c$ is close to 0°, the wetting is in Cassie impregnating state as Ineq. 2-15 is met and also according to Eq. 2-14, $\theta_a$ is close to 0°. Now we consider the possibility to create the superwetting surface when $\theta_c$ has a relatively large value. It is easy to make Ineq. 2-15 satisfy as observed from Eq. 2-10 and Figure 2-4 and Figure 2-5, since $\theta_1$ can be increased. For example $\theta_1$ can be increased by using high aspect ratio roughness structures. This can be done by keeping $f$ fixed by fixing the top area of the structures and increasing $r$ by increasing the height of the structures.

By Eq. 2-14, Figure 2-6 and Figure 2-7 give the relation of $\theta_a$ and $f$ when the values of $\theta_c$ are fixed to 40° and 80°. It is observed from Figure 2-7, to make $\theta_a$ less than

5°, $f$ should be smaller than 0.013 and 0.005 when $\theta_c$ is 40° and 80° respectively. It implies that, when $\theta_c$ is 40° or above, to make $\theta_a$ less than 5°, $f$ should be at least less than 0.013 and the required value of $f$ decreases with increase in $\theta_c$.
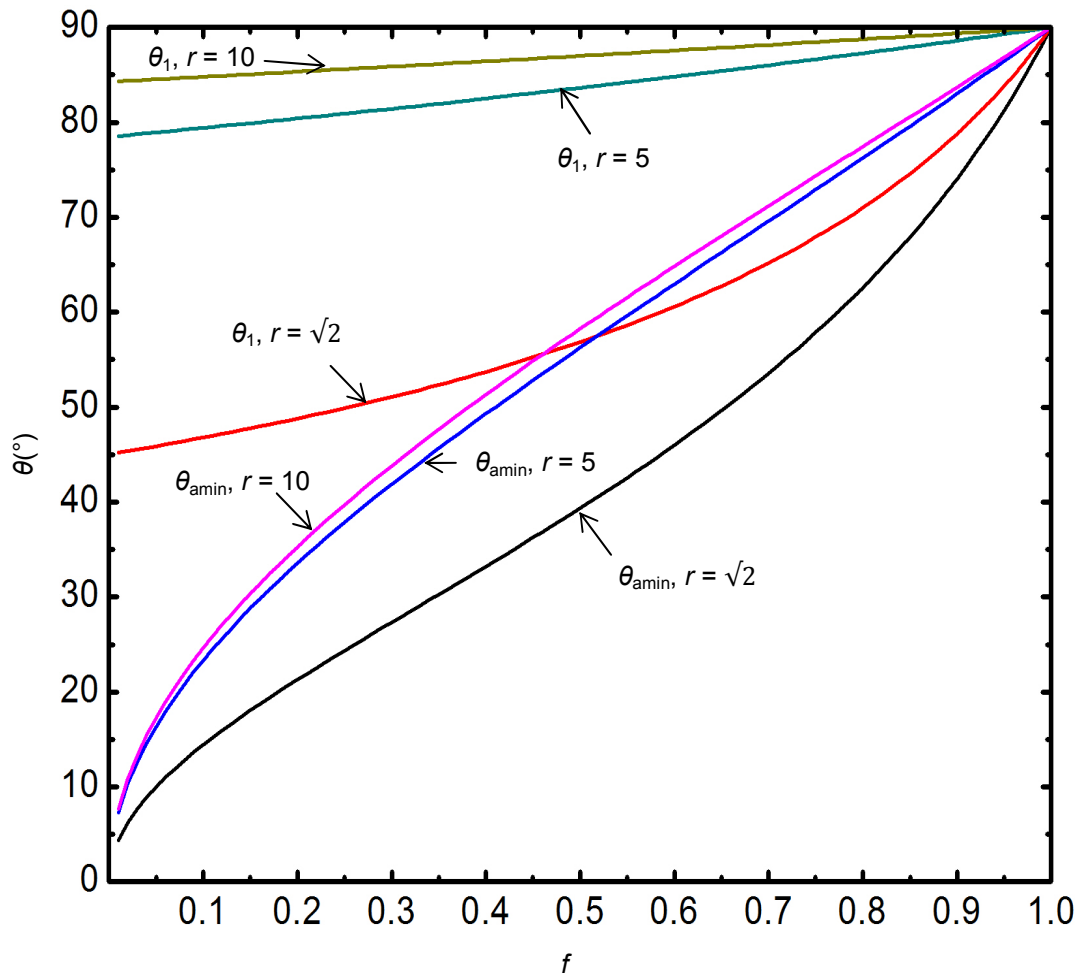


Figure 2-4: Variations of $\theta_1$ and $\theta_{amin}$ with the large values of $f$ for different values of $r$.
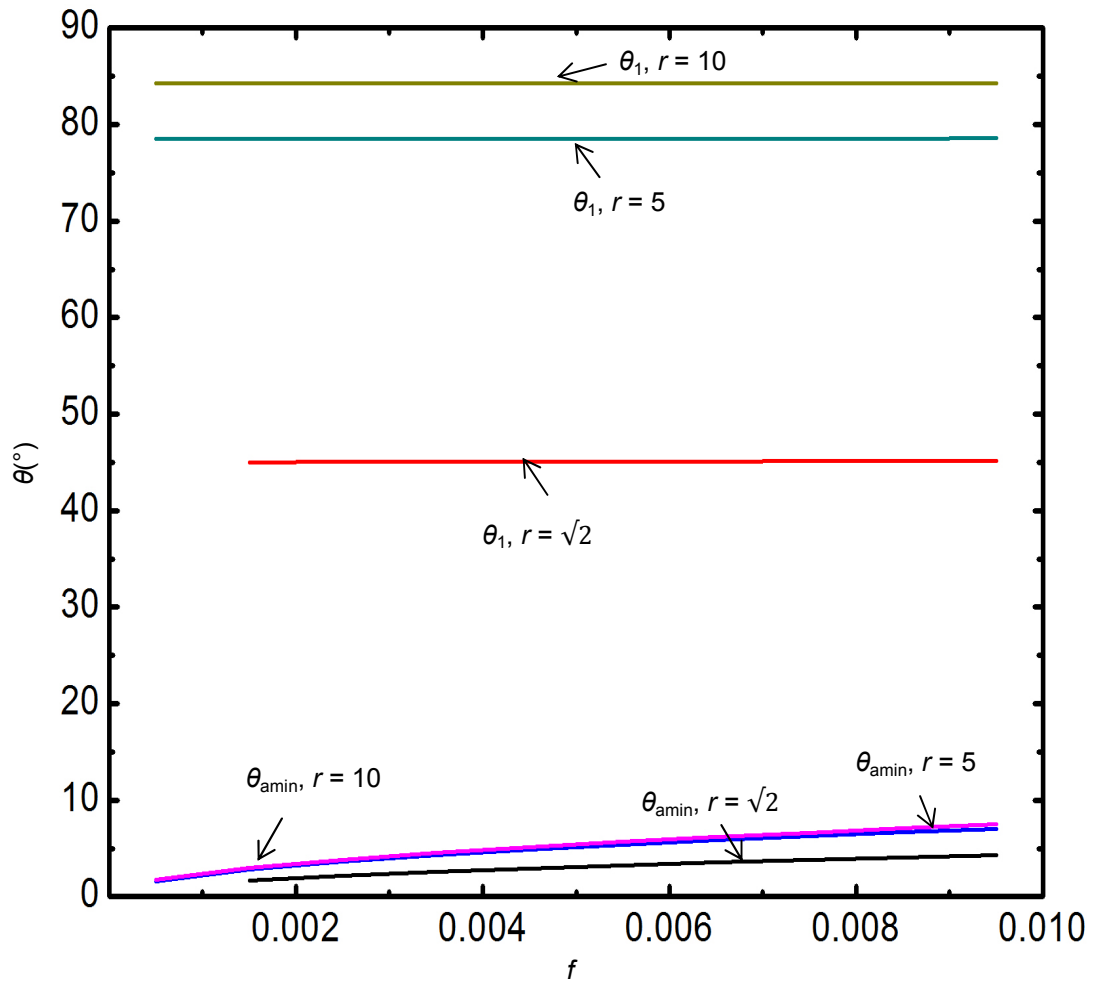
Figure 2-5: Variations of $\theta_1$ and $\theta_{amin}$ with the small values of $f$ for different values of $r$.
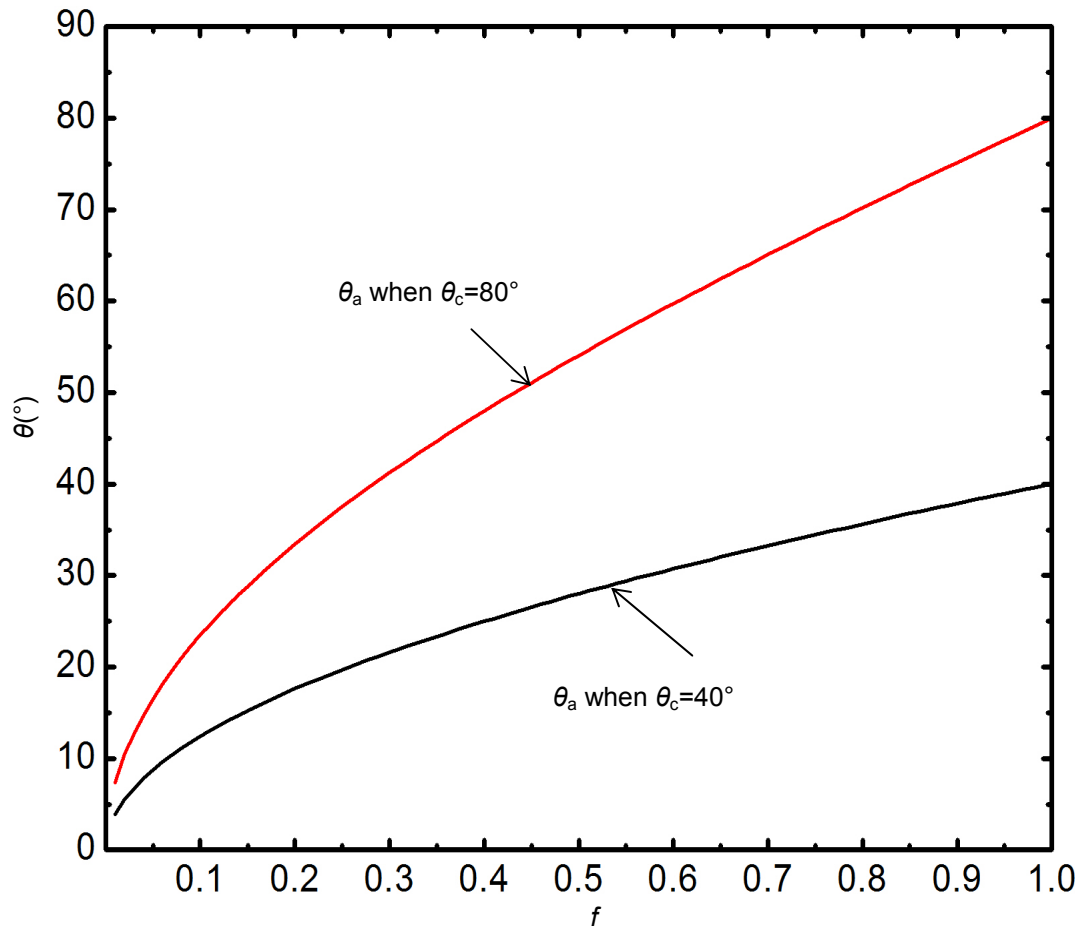
Figure 2-6: $\theta_a$ -$f$ relations when the values of $\theta_c$ are 40° and 80°, respectively.
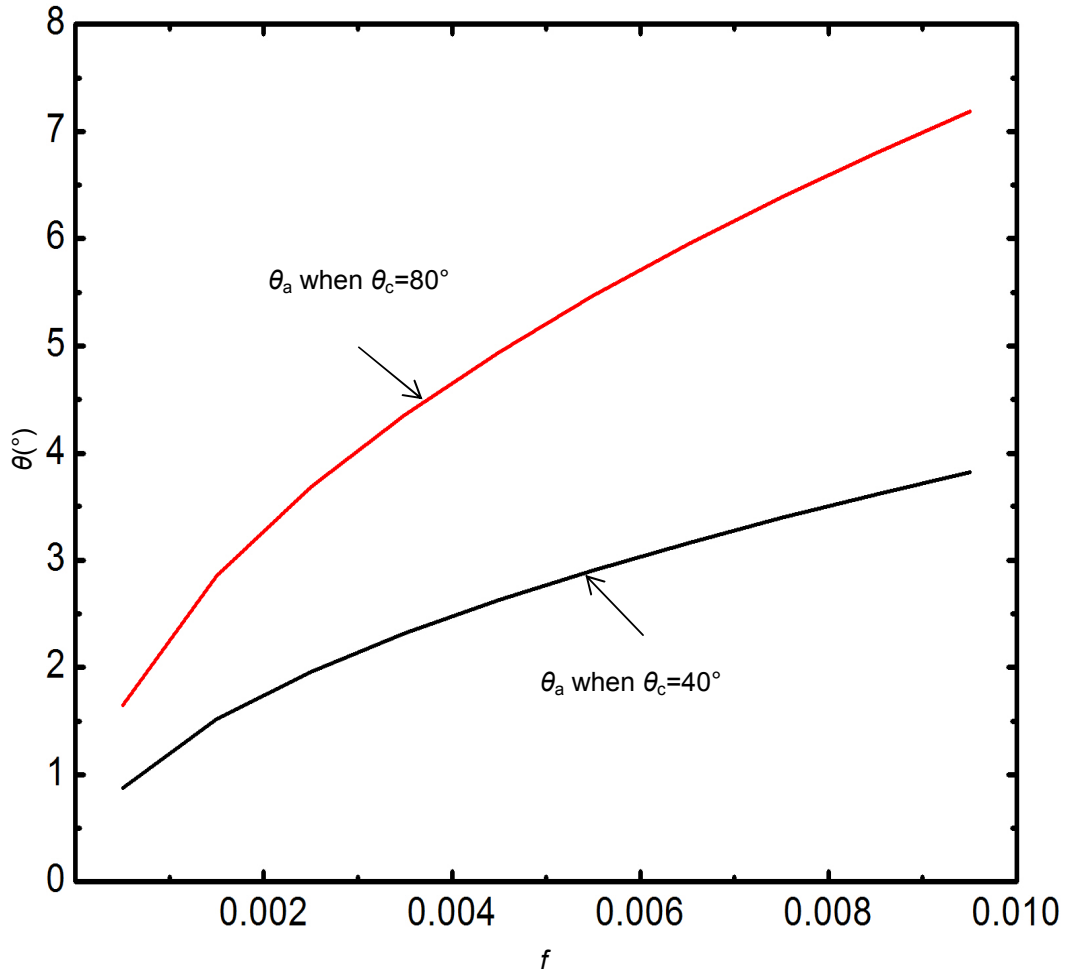
Figure 2-7: $\theta_a$ -$f$ relation when the values of $\theta_c$ are 40° and 80°, respectively.

Chapter 3

Design of Roughness Structures

Various structures can be adopted to change the wetting property of a given surface. Often pillar or channel like structures is adopted. In this work our goal is to create superwetting surfaces with apparent contact angle less than 5° ($\theta_a < 5°$). Hence according to the discussion in chapter 2, to make $\theta_a$ less than 5° either in Wenzel or Cassie impregnating state when $\theta_c$ is 40° or above, the critical point is to have the corresponding $f$ at least less than 0.013. This can be achieved in various ways. For example, If only micro or nanopillars are used, in either case the distance between the two neighboring pillars should be at least 8 times the width of the pillars in order for $f$ to be less than 0.013. In this way the roughness structures will be sparsely spaced (Figure 3-1) and may not create superwetting surfaces as seen in Figure 3-2.



Figure 3-1: SEM image of top view of sparsely spaced micropillars.

An extreme example that may support this concern is that, when $f$ is 0.00001, which means that the pitch is about 100 times the width of the pillar, In this case the roughness structures should have little influence on the wetting of the surface. Therefore the use of only micro or 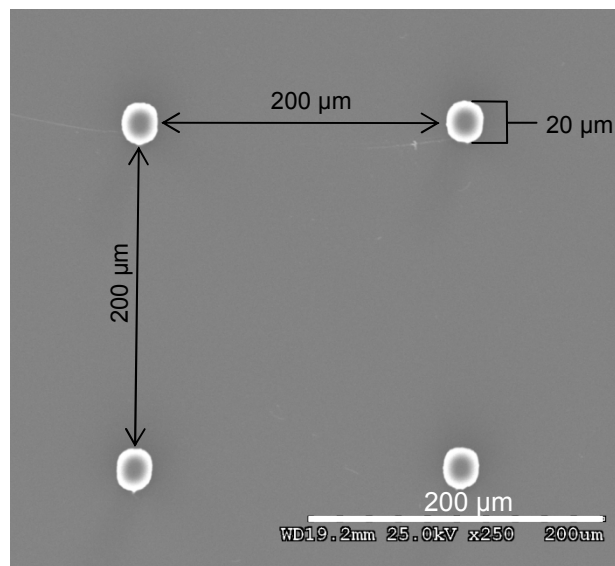nanostructures may not necessarily create a superwetting state. Consequently, hybrid micro/nanostructures, which is nanostructures covered microstructures are chosen in this work to generate superwetting surfaces.

As discussed earlier, we have to create roughness structures such that $f$ is at least less than 0.013. Set $f_m$ to be the ratio of the top surfaces of the micropillars over the projected surface area and let $f_n$ be the ratio of the top surfaces of the nanopillars over those of micropillars. According to [17], we have

$$f = f_m f_n, \qquad\qquad (3\text{-}1)$$

According to this equation, if both $f_m$ and $f_n$ are less than 0.115, then the resulting $f$ will be less than 0.013. This can be achieved when the pitches in either micro- or nanopillars are not less than twice the lateral dimensions of the corresponding pillars.
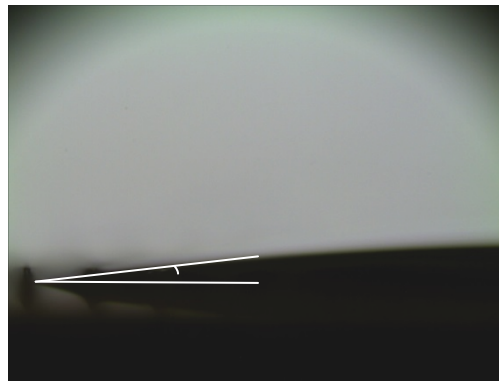


Contact Angle = 9°

Figure 3-2: Side view of a liquid drop placed on sparsely spaced micropillars.

3.1 Calculation of Surface Roughness Factor and the Solid Fraction

The roughness factor $r$ is the ratio of the actual surface area of the rough surface, $A_h$, to the projected surface area, $A_f$, given by: [23-25]

$$r = \frac{A_h + A_f}{A_f} = 1 + \frac{A_h}{A_f}.$$

(3-2)

The solid fraction $f$ is the ratio of the top surface area of the rough surface, $A_t$ to the projected surface area, $A_f$, given by:

$$f = \frac{A_t}{A_f}.$$

(3-3)

*3.1.1 Roughness Factor and Solid Fraction for Square Pillars*

For a regular squared pillar array with a pillar size $a$ x $a$, spacing $b$, and a height $h$, the surface roughness, $r_{sq}$, can be calculated by,

$$r_{sq} = 1 + \frac{4ah}{(a+b)^2},$$

(3-4)

where $A_f = (a + b)^2$ and $A_h + A_f = 4ah + a^2 + 2ab + b^2$.

Solid fraction for a regular square pillar array, $f_{sq}$, with a pillar size $a$ x $a$ on a total projected area $A_f$, is calculated by:

$$f_{sq} = \frac{a^2}{(a+b)^2}.$$

(3-5)
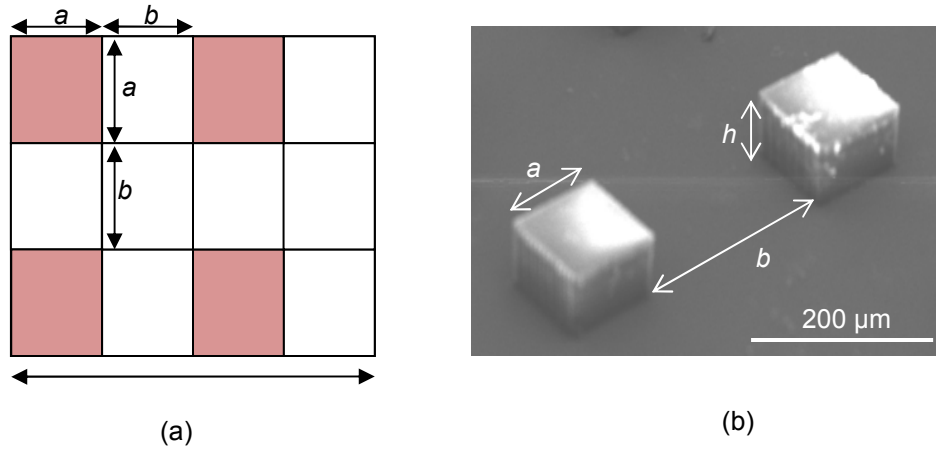
Figure 3-3: (a) Schematic top view of the square micropillars. (b) SEM image of the micropillar array.

*3.1.2 Roughness Factor and Solid Fraction for Hexagonal Nanowires*

In our case, the fabrication of ZnO nanowires was done using a hydrothermal approach, thereby not achieving a regular array. To estimate the *r* and *f* for ZnO nanowires, we had to consider a projected area ($A_f$) on the SEM image, which in our case was considered to be 5 x 5 µm$^2$. Average diameter (*a*), side length (*c*) and height (h) of the ZnO nanowires were calculated which were inside the projected area.

The roughness factor for the Hexagonal ZnO nanowires, $r_{hx}$, is calculated by:

$$r_{hx} = 1 + \frac{n6ch}{A_f},$$  (3-6)

where *n* is the total number of nanowires in the projected area, $A_f$ is the projected area.

The solid fraction for the hexagonal ZnO nanowires, $f_{hx}$, is calculated by:

$$f_{hx} = \frac{n\frac{3\sqrt{3}a^2}{2}}{A_f},$$  (3-7)

where the numerator gives the total number ($n$) of nanowires in the projected area times the area of the top surface of the hexagonal ZnO nanowires.

Projected area



(a)

(b)



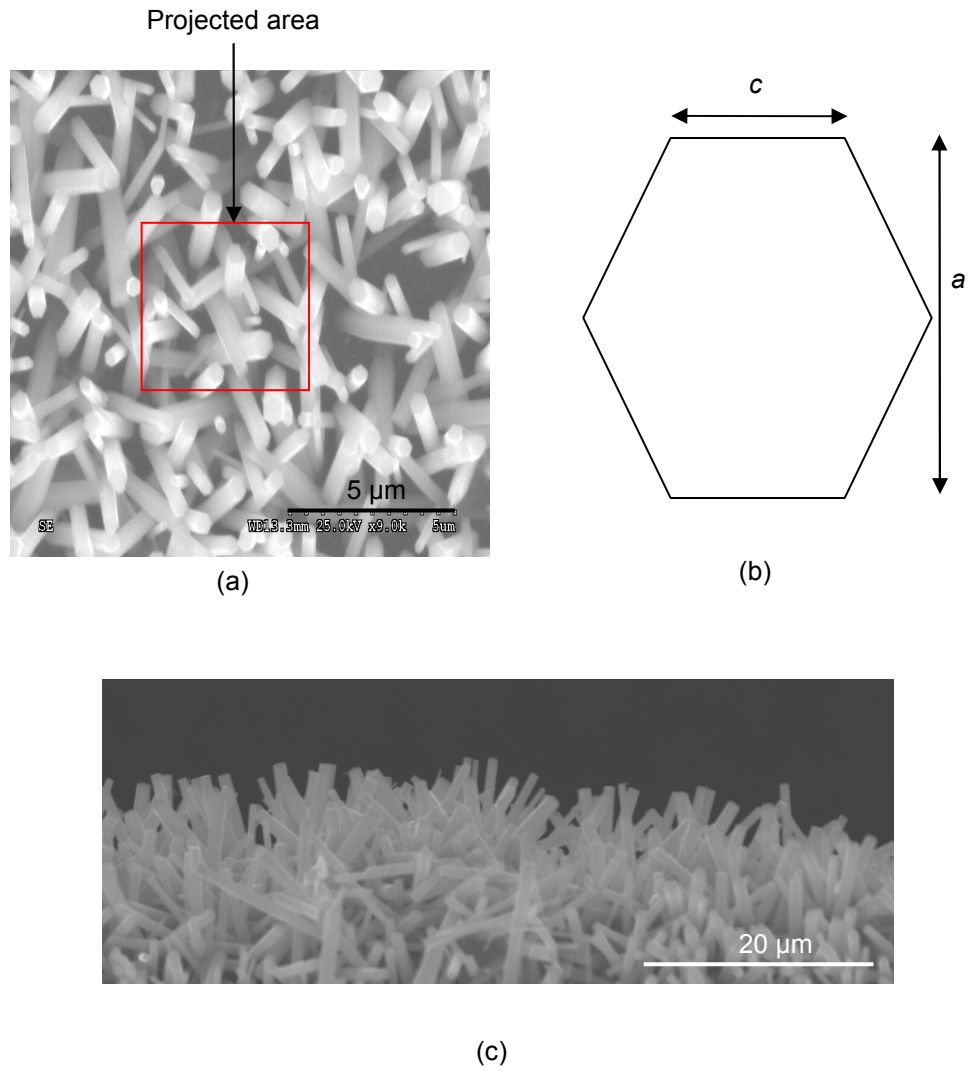(c)

Figure 3-4: (a) SEM image of the ZnO nanowires. (b) Schematic top view of a ZnO nanowire. (c) Side view SEM image of ZnO nanowires.

Chapter 4

Fabrication

Totally five types of samples were fabricated and tested in this work. The fabrication process for each type of sample is described in this chapter.
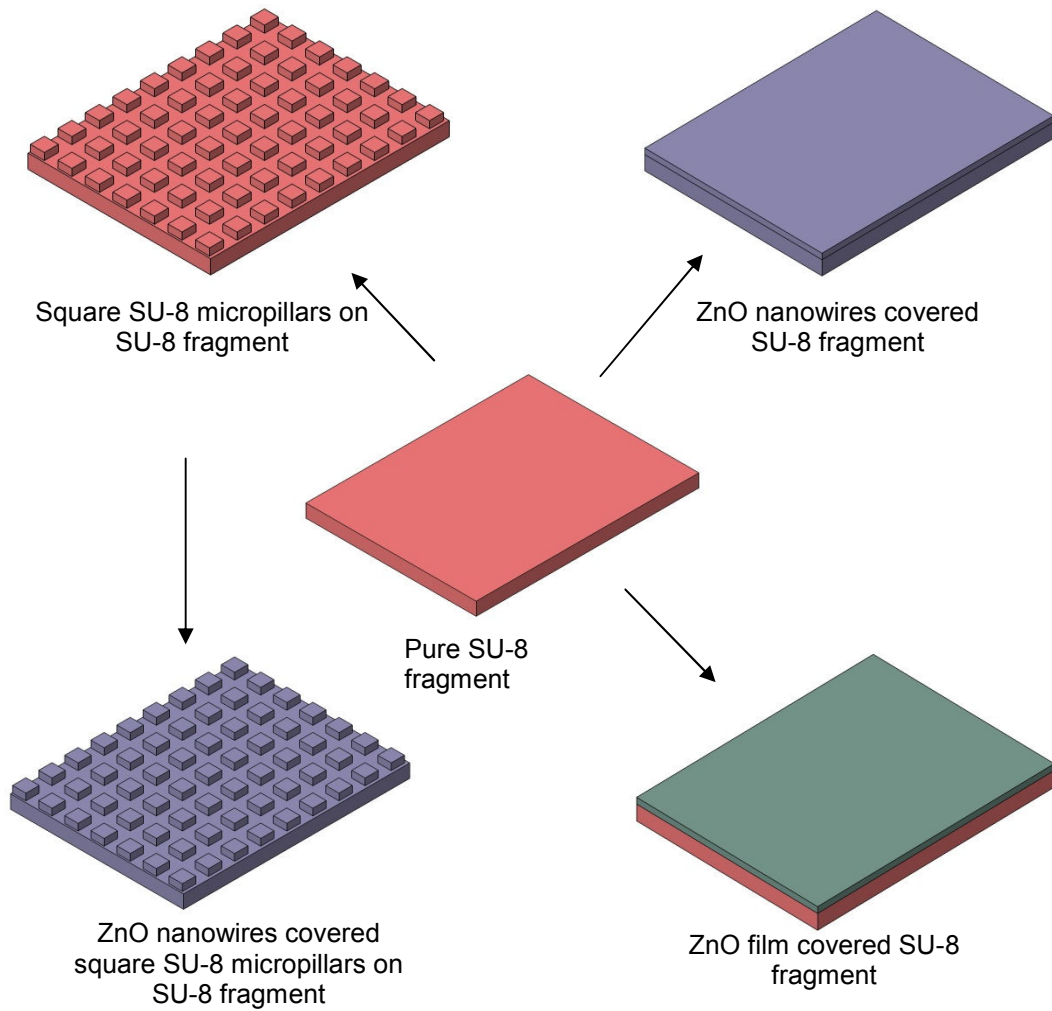


Figure 4-1: Schematic representation of the processing sequence of the five samples.

## 4.1 Fabrication of a Pure SU-8 Fragment

SU-8 is a negative photoresist and was chosen to fabricate a pure fragment, as well as micro pillars, due to two reasons. First, using ultra-violet (UV) lithography, SU-8 can be patterned to desired shapes and its thickness can also be controlled. It has been widely used in the MEMS area for various structures, such as gears [26], boats [9], and flotillas [8]. Second, the density of SU-8 is 1.16 x $10^3$ Kg/m$^3$, higher than those of IPA and water. This meets the requirement that a small plate should be denser than the liquid, which makes the small plate sink after the effect of surface tension is eliminated. SU-8 100 and SU-8 25 (Microchem Co.) are used to fabricate pure fragments and micropillars, respectively. These two SU-8 materials differ in their viscosities. SU-8 100and 25 have viscosities of 51,500 and 2,500 centistokes, respectively, making them suitable for manufacturing structures with the thicknesses in the orders of 100 and 10 μm.

The fabrication of pure SU-8 fragments is as follows:

1. Spin-coat SU-8 100 on silicon wafer at 300 rpm for 60 s to achieve a desired thickness of 100 μm.

2. Pre-bake the sample on a hot plate at 65°C for 10 min followed by a 30 min soft bake at 95°C.

3. Expose the SU-8 sample, after it cools down, to UV light through a mask with the desired pattern for 27 s in a mask aligner. The exposure energy required for 100 μm thickness is around 540 mJ/cm$^2$ and the backside aligner used for exposure has been calibrated to 20mW/cm$^2$.

4. Bake the sample at 65°C for 1 min followed by baking it at 95°C for 10 min.

5. Develop the sample in SU-8 developer for 10 min.

6. Rinse the sample with IPA and immerse it in the developer. Repeat this cycle several times till the white residue fades away.

7. Finally rinse the sample with DI water and dry it with nitrogen.



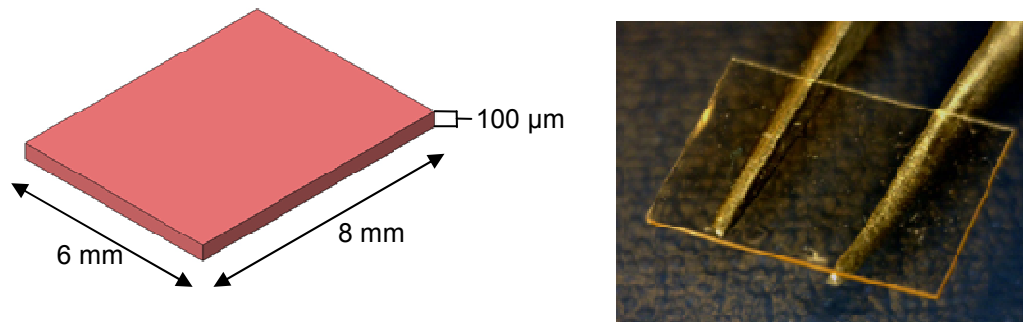Figure 4-2: Schematic diagram of SU-8 fragment (left) and perspective view of a fabricated sample (right).

## 4.2 Fabrication of a ZnO Film on a PureSU-8 Fragment

A pure SU-8 fragment was taken as a substrate, and a ZnO film was sputtered on this fragment for 30 min using a sputtering machine. [27]
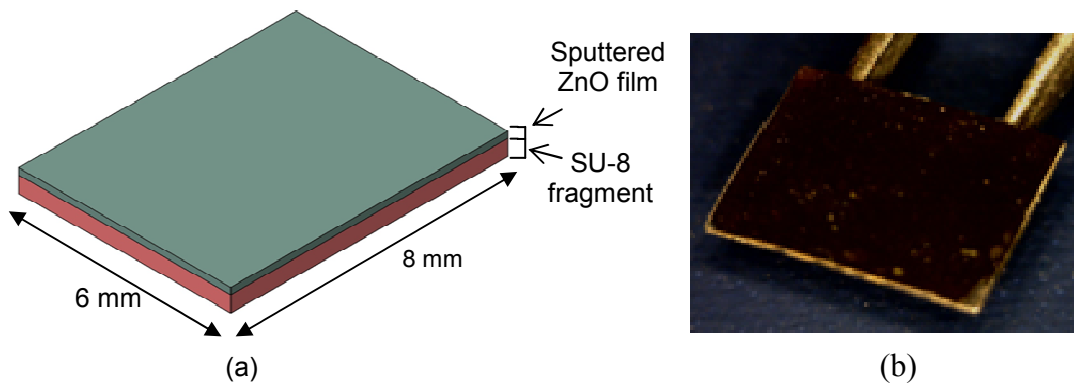


Figure 4-3: (a) Schematic diagram of SU-8 fragment coated with a ZnO film, and (b) perspective view of a fabricated sample.

## 4.3 Fabrication of ZnO Nanowires on a Pure SU-8 Fragment

Again, a pure SU-8 fragment was taken as a substrate, and ZnO nanowires were fabricated on the fragment using a hydrothermal growth method [28] as follows:

1. Prepare a ZnO nanocrystal solution by mixing 0.044 g zinc acetate dehydrate in 20 ml 1-propanol.

2. Dip the substrate in this solution for 15 min.

3. Prepare a growth solution by mixing 0.727 g zinc nitrate hexahydrate and 0.35 g hexamethylene tetramine in 200 ml DI water.

4. Put the substrate facing down inside the growth solution and heat the solution at 80°C for 3 hrs.

5. Take the sample out and gently rinse it with DI water.
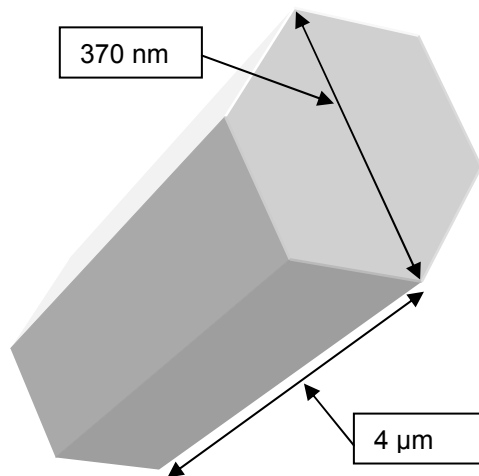


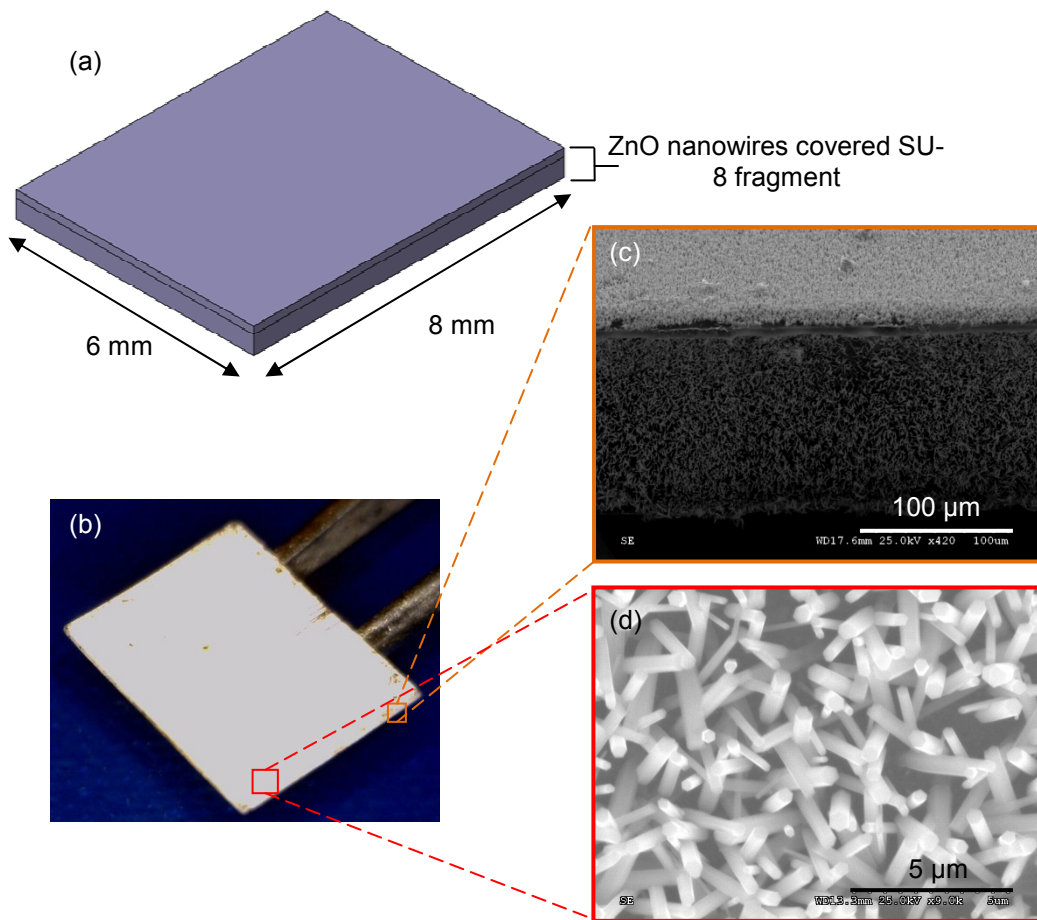370 nm

4 µm

Figure 4-4: Schematic view of a ZnO nanowire.

Figure 4-5: (a) Schematic diagram of an SU-8 fragment that is coated with ZnO nanowires. (b) Perspective (optical) view of the fabricated sample. (c) and (d) close-up (SEM) views of ZnO nanowires on the SU-8 fragment.

## 4.4 Fabrication of SU-8 Square Micropillars on a Pure SU-8 Fragment

SU-8 square micro pillars were fabricated on a pure SU-8 fragment. SU-8 25 having a viscosity of 2500 cSt was chosen to fabricate the micro pillars as the desired thickness of micro pillars was 25 µm. The fabrication process is as follows:

1. Spin-coat SU-8 25 on the SU-8 fragment at 2000 rpm for 30 s.

2. Pre-bake the sample at 65°C for 3 min followed by soft bake at 95°C for 7 min.

3. Expose the sample, after it cools down, to UV light through a mask with desired patterns for 12.5 s in a mask aligner. The energy required for 25 µm thickness is 250 mJ/cm$^2$, and the backside aligner used for the exposure is calibrated to 20 mW/cm$^2$.

4. Bake the sample at 65°C for 1 min followed by hard bake at 95°C for 3 min.

5. Develop the sample in SU-8 developer for 4 min followed by several cycles of IPA rinse till white residue fades away.

6. Rinse the sample with DI water and dry it using compressed nitrogen.

(a)

Micropillar

25 µm

100 µm

8 mm

6 mm

SU-8 fragment

(b) 100 µm

200 µm

200 µm

100 µm

(c)

(d)

500 µm
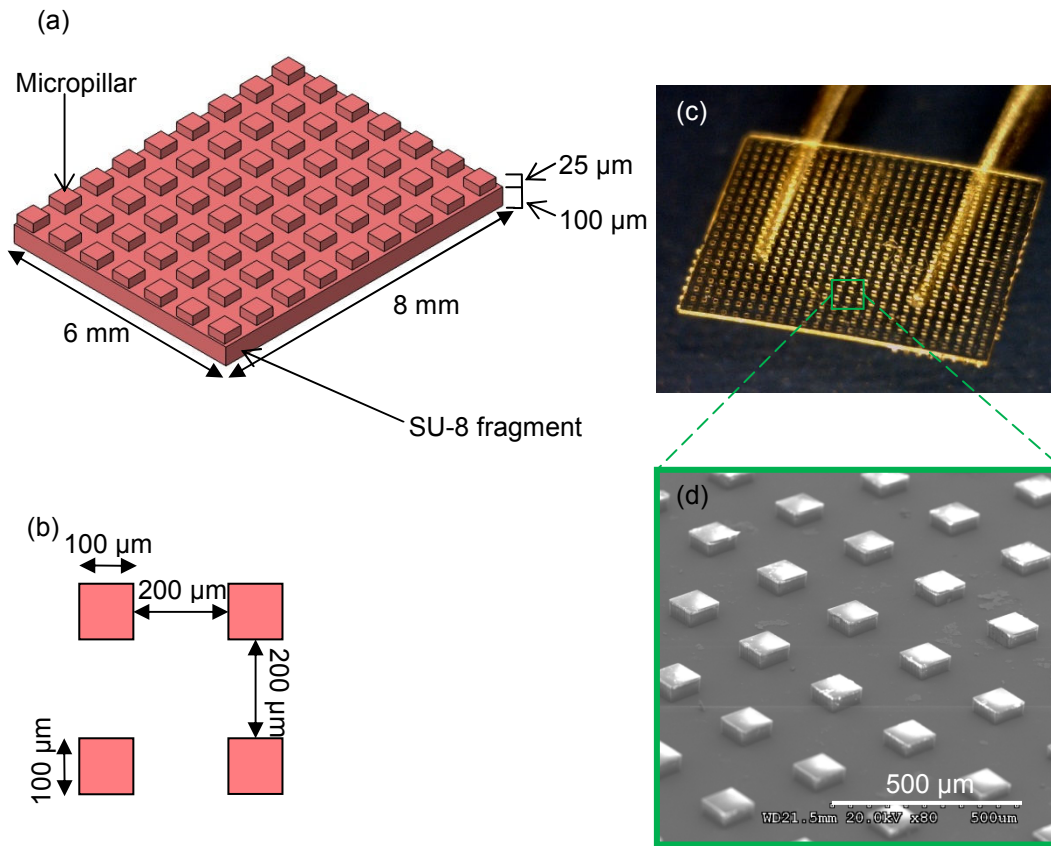
WD21.5mm 20.0kV x80    500um

Figure 4-6: (a) Schematic diagram of SU-8 micropillars on SU-8 fragment. (b) Top view showing the dimensions of the micropillars. (c) Perspective view of the fabricated sample. (d) SEM image of the SU-8 micropillars.

## 4.5 Fabrication of ZnO Nanowires Covered SU-8 Square Micropillars on a Pure SU-8 Fragment

ZnO nanowires covered SU-8 micropillars were fabricated on a pure SU-8 fragment using the fabrication techniques discussed earlier in this chapter.
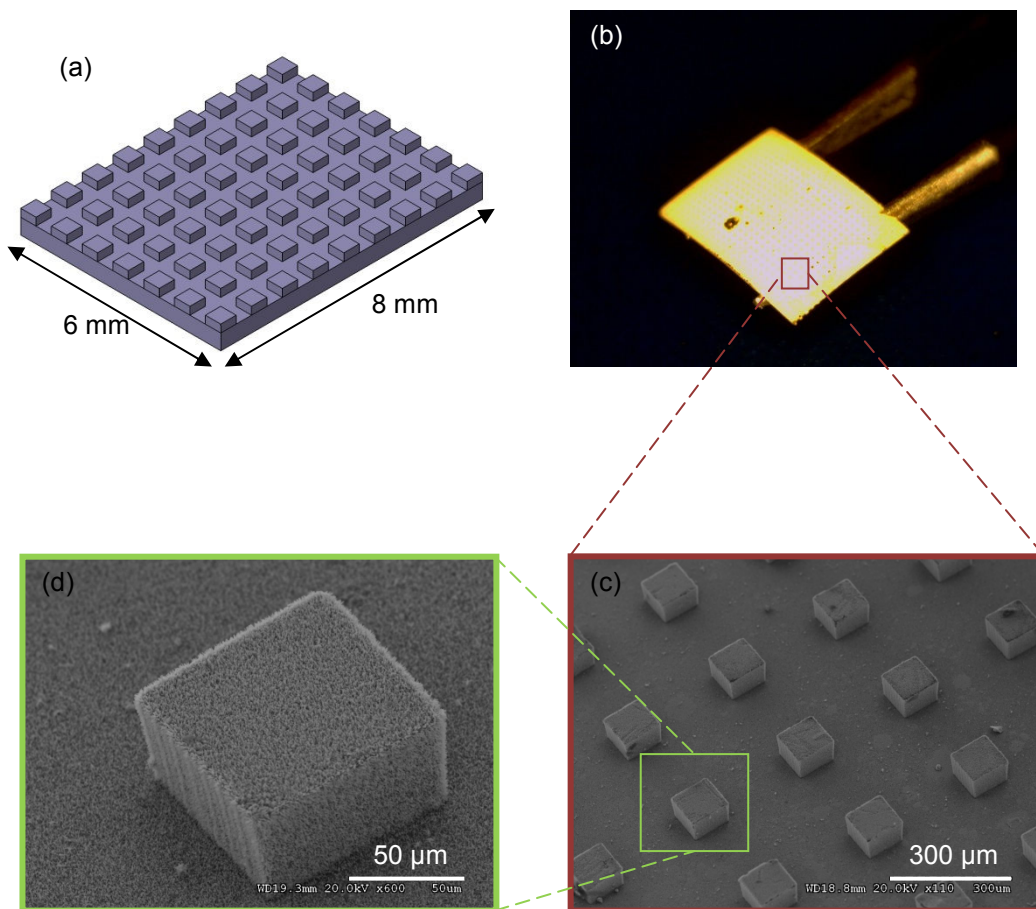


Figure 4-7: ZnO nanowires covered SU-8 micropillars on SU-8 fragment. (a) Schematic diagram. (b) Perspective (optical) view. Close-up (SEM) views of (c) an array of micropillars and (d) a single micropillar.
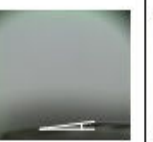
Chapter 5
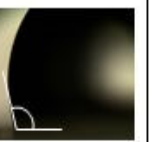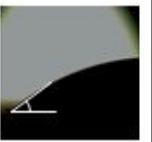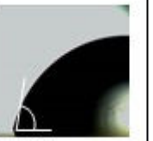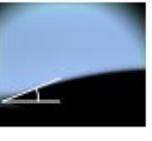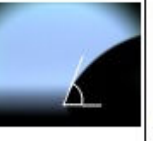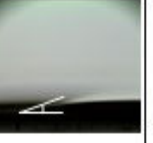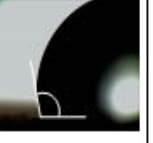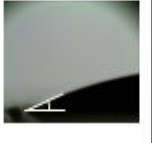
Results and Discussions

5.1 Tested Structures

For the purpose of comparison and analysis of wetting states, a total of five types of samples were fabricated as listed in Table 5-1 and also mentioned below:

i.      Type 1 sample: ZnO nanowires covered SU-8 micropillars were created on the top surface of an SU-8 fragment with the dimensions of 8 mm x 6 mm x 0.1 mm (length x width x thickness). The width, thickness and spacing of the SU-8 micropillars are 100 μm, 25 μm and 200 μm respectively. While the average diameters, pitches and heights of the ZnO nanowires were 0.37 μm, 0.3 μm and 4μm respectively.

ii.     Type 2 sample: Pure SU-8 fragment having length, width and thickness of 8 mm, 6 mm and 0.1 mm respectively.

iii.    Type 3 sample Pure: ZnO film sputtered on SU-8 fragment having the same dimension as mentioned in the type 2 sample.

iv.     Type 4 sample: ZnO nanowires were fabricated on SU-8 fragment using hydrothermal approach. The average diameters, pitches and heights of the ZnO nanowires were 0.37 μm, 0.3 μm and 4μm respectively.

v.      Type 5 sample: Square SU-8 micro pillars with dimensions 100 μm, 25 μm and 200 μm ( width, thickness and spacing) were fabricated on SU-8 fragment having dimensions 8 mm, 6 mm and 0.1 mm (length, width and thickness).

34

Table 5-1: Testing of liquids with various concentrations on different samples. An equilibrium state is shown in each optical image. The angle given underneath an image represents advancing intrinsic or apparent contact angle, not the equilibrium contact angle in the image. The error of the measured contact angles is 2°.

| Solutions / Samples | 100% IPA | 75% IPA 25% Water | 50% IPA 50% Water | 25% IPA 75% Water | 100% Water |
|---|---|---|---|---|---|
| Type I: ZnO nanowires-covered SU-8 square micropillars ($f=0.012$, $r=7.58$) | 0° | 0° | 0° | 7° | 104° |
| Type II: Pure SU-8 fragment ($f=1$, $r=1$) | 0° | 18° | 33° | 46° | 80° |
| Type III: ZnO films ($f=1$, $r=1$) | 9° | 22° | 40° | 66° | 92° |
| Type IV: ZnO nanowires ($f=0.11$, $r=6.47$) | 0° | 8° | 11° | 18° | 103° |
| Type V: SU-8 square micropillars ($f=0.11$, $r=1.11$) | 0° | 6° | 23° | 38° | 76° |

Various testing solutions were prepared by mixing different concentration (mass) of de-ionized water and Isopropyl alcohol and were tested on the five types of samples mentioned earlier. Fixed volume of the liquid solutions were put on the samples using Hamilton 80300 microlitre syringe pump and the corresponding equilibrium states were observed through an optical microscope as mentioned in Table 5-1.  Advancing apparent contact angles were measured on samples using the corresponding solution and tabulated in Table 5-1. For the Type 2 and 3 samples, the advancing apparent contact angles were also the advancing intrinsic contact angle for themselves and also for the other 3 types of samples. It was observed that contact angles increased with the decrease in the IPA concentration in the solution.

<div align="center">5.2 Superwetting surfaces and wetting states</div>

To create superwetting surfaces, three approaches are available as discussed earlier in Chapter 2 in the theoretical modeling section. These results were validated by the contact angle results tabulated in Table 5-1. These approaches are listed below:

1) It is possible to create superwetting surfaces when the intrinsic angle ($\theta_c$)  itself is 0°, which is in the case of second and fifth types of samples when the testing solution used was 100% IPA.

2) When the intrinsic angle ($\theta_c$) is small, it will still result in superwetting surfaces by incorporating roughness structures with relatively large $f$ on the corresponding samples. For example, in the case of type 4 sample, whose $f$ is 0.11, the $\theta_a$ is 0° when 100% IPA is used as the testing solution. $\theta_c$ for the corresponding sample is 9° with the same solution.

3) When the intrinsic contact angle ($\theta_c$) is relatively large while having $f$ smaller than 0.013.

<div align="center">36</div>

In this work we have particularly explored the superwetting surfaces created when the intrinsic contact angle is relatively large while having $f$ less than 0.013. In the type 1 sample, which includes ZnO nanowires covered SU-8 micro pillars and whose $f$ is 0.012, $\theta_a$ is 0° when the testing solution is 50% IPA which the corresponding $\theta_c$ to be 40°. When the IPA concentration was lowered and was less than 50%, superwetting surface may not be created as $\theta_a$ may be above 5°. For instance, when the testing solution is 25% IPA with the corresponding $\theta_c = 66°$, the $\theta_a$ was measured to be 7°, which is more 5°, thus not creating superwetting surface. Using Eq. 2-10 , $\theta_1$ was calculated to be 82°, which is more than the intrinsic contact angle, thus the wetting is in the Cassie impregnating state. Also the experimentally measured value of $\theta_a$ was validated using Eq. 2-14, where θa was calculated to be 7°, which is the same as the measured one. It was also observed in the type 4 and 5 samples, that superwetting surfaces are not created when the testing solution was 50% IPA. The corresponding values of $\theta_a$ were 11° and 23° respectively. The two samples include only ZnO nanowires or SU-8 micropillars, and their values of $\theta_c$ are 40° and 33° respectively. In both the samples, the corresponding values of $f$ are 0.11, which is not small enough to make the surface superwetting on these samples. Thus the experimental results indicate that the third approach is capable of producing superwetting surfaces as predicted in the Chapter 2.

It was also observed from the Table 5-1, that when only water was used as the testing solution, the $\theta_a$ on the type 1 sample was 104°, with the corresponding $\theta_c$ to be 92°. The wetting was in Wenzel state. The value of $\theta_a$ was validated using Eq. 2-8, which predicts that the roughness structures will enhance the surface hydrophobicity if the intrinsic contact angle is more than 90°.

5.3 Spreading Tests

Spreading of liquids having various concentrations of IPA was observed on the samples containing the roughness structures. Each time before testing, the sample was cleaned with pure de-ionized water and dried with compressed air. The sample was kept on a leveled surface under the optical microscope which was attached to the FASTEC IMAGING TS3 high speed camera for the observation of the liquid front propagation. The camera was set up above the sample at an angle of 90°. Deposition of test liquid was performed using a 10.0 µl Hamilton 80300 syringe pump. A volume of 5.0 µl of test liquid was deposited on the top of the sample each time and liquid front propagation was observed at 1250 fps. All experiments were done under room temperature of 21.0°C ± 2.0°C. Mixtures of IPA and DI water were made with varying concentrations of IPA. In Fig. 8, the top view images of the spreading meniscus of the fluid having a concentration of 10% IPA – 90% water at different stages of propagation are observed. The spreading direction was from left to right as marked by an arrow in the figure. As observed from Figure 5-1 (a), when a 5 µl drop of liquid containing 10% IPA was placed on the type 1 sample, the liquid front propagated together covering all the three SU-8 micro pillars at the same time. The micropillars were fully submerged in liquid thus not creating any islands. As observed in Figure 5-1 (b), the liquid front finally got pinned at the corners of the micropillars creating the meniscus shape bending outwards to the air side, which stopped the further spreading of the liquid. The wetting was in the Wenzel state. The wetting state was also observed using top and side view optical microscope. $\theta_c$ was measured to be 85° which is larger than the critical angle $\theta_1$, which was 82°. Accordingly the observed wetting state matched the theoretical prediction. On the other hand it was observed that when the concentration of the liquid was changed to 50% IPA, and 5 µl drop of the corresponding liquid was placed on the type 1 sample, the spreading behavior

38

was different. There was a thin film of the liquid which was propagating between the micro pillars thus exposing the top surface of the pillars to air. The liquid front moved at the same speed between the neighboring sets of pillars as observed in Figure 5-2 (a), but as observed from Figure 5-2 (b), when the part of this liquid front reached the top pillar, it quickly spread along the edges and corners of the pillars. It further passed the micro pillar and kept spreading further. The direction of spreading was from left to right as marked in the Figure 5-2. Meanwhile the part of the liquid front did not reach the bottom micropillar, thus forming a discontinuity in the front and not forming a meniscus between the micropillars. Also through both the top and side view optical microscope, the wetting state was observed to be in Cassie impregnating state which was also validated using the theoretical prediction.

Through these spreading tests, propagation of the liquid fronts were observed in different wetting states. The liquid penetration speed in between the roughness structures varied in the two wetting states. In the case when $\theta_c < \theta_1$, which was the Cassie impregnating state, the liquid front was spreading quickly in between the roughness structures and also at different time instants in between the two neighboring pillars. Thus not reaching an equilibrium state between the two neighboring roughness structures which resulted in continuous spreading in between the roughness valleys. On the other hand, when $\theta_c > \theta_1$, the spreading process slowed down at the roughness structure edges and the liquid front passed the two neighboring roughness structures at the same time, thus making it possible to form an equilibrium state and forming a meniscus which resulted in pinning of the liquid front in between the roughness structures.

Figure 5-1: Propagation of a liquid with 10% IPA and 90% water on ZnO nanowire-covered micropillars (high-speed camera images taken at 1250 fps). (a) The liquid front gets into the valley between micropillars, and (b) it stops spreading when it contacted the right corners of the micropillars, forming a shape bending towards the air side.
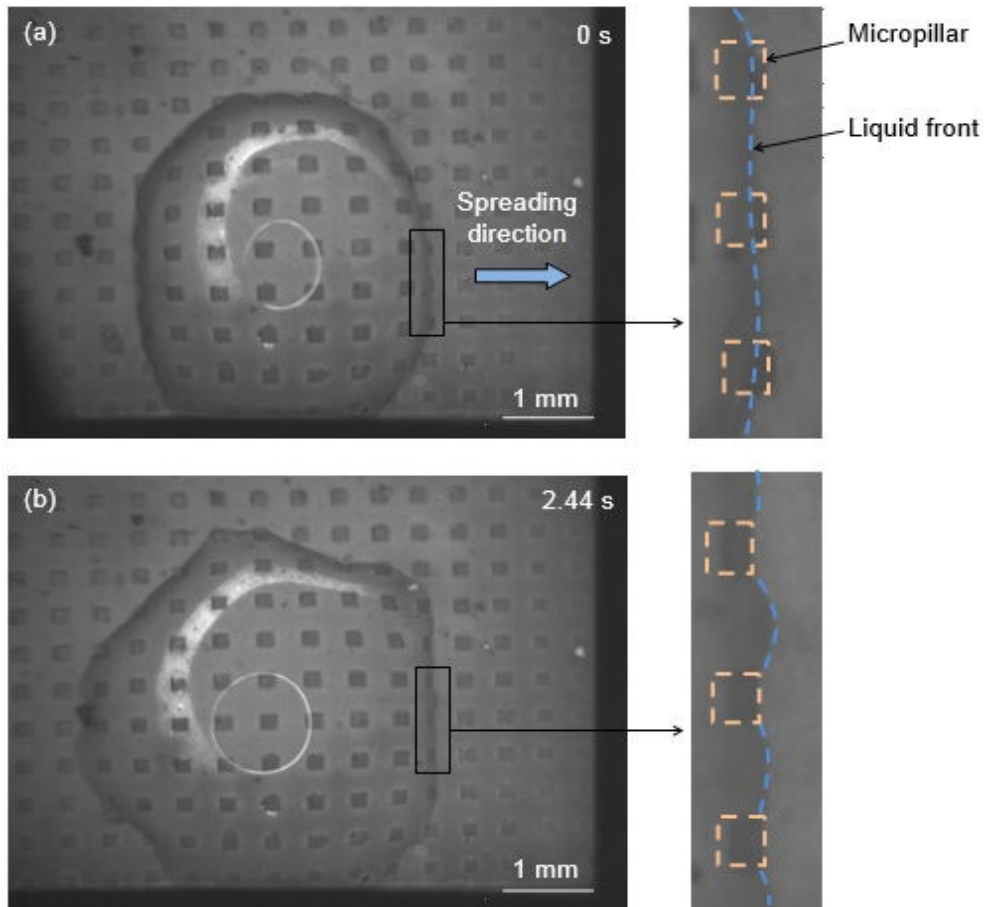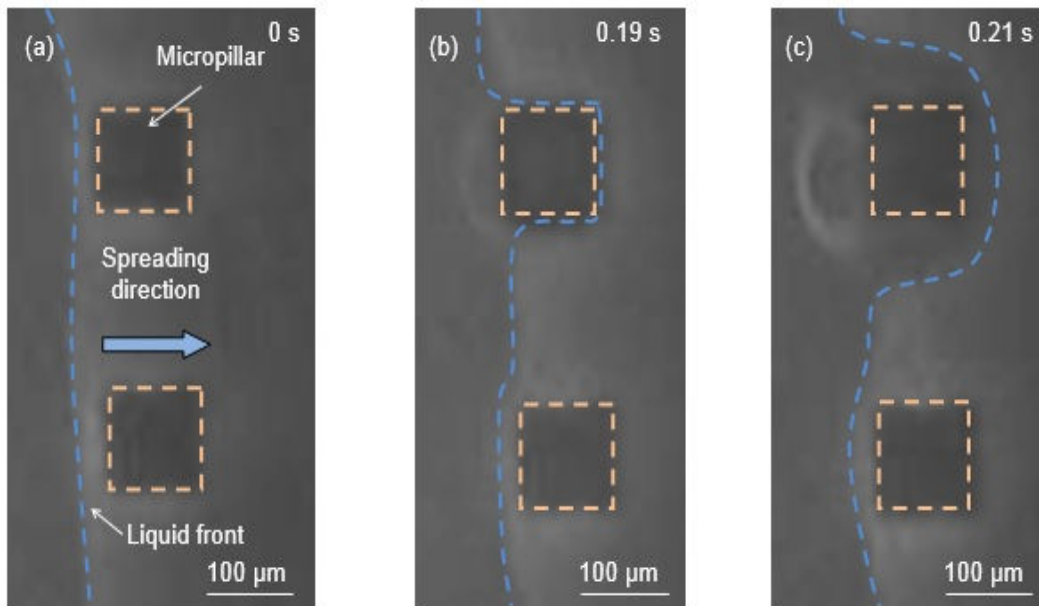
Figure 5-2: Propagation of a liquid with 50% IPA and 50% water on ZnO nanowire-covered micropillars (high-speed camera images taken at 1250 fps). (a) The liquid front approaches the micropillars from the left to right, (b) it spreads along the edges of the top micropillar, and (c) it continues to spread after passing the top micropillar.

## 5.4 Sinking Tests

The sinking tests were conducted to observe the sinking of the sample which was placed in the liquid. The liquid was prepared by thoroughly mixing the desired volume of IPA and water together in a container. All the experiments were done at the room temperature. It was observed that the samples having the corresponding superwetting surfaces sank to the bottom of the container, while the ones without did not sink at all. As observed in Figure 5-3, when the type 1 sample with the superwetting surfaces facing up was gently kept on the liquid having 50% IPA using tweezers, the sample sank completely to the bottom of the liquid. It took the sample about 6.5 s to completely sink to the bottom. On the other hand when the sample was put on the liquid surface with the superwetting surface facing down or the untreated surface facing up, it did not sink at all even though it was slightly pressed with the tweezers as seen in Figure 5-4. The difference in the testing results indicates that the creation of the superwetting surface using ZnO nanowires-covered SU-8 micropillars made it possible to eliminate the effect of surface tension on the SU-8 fragments.
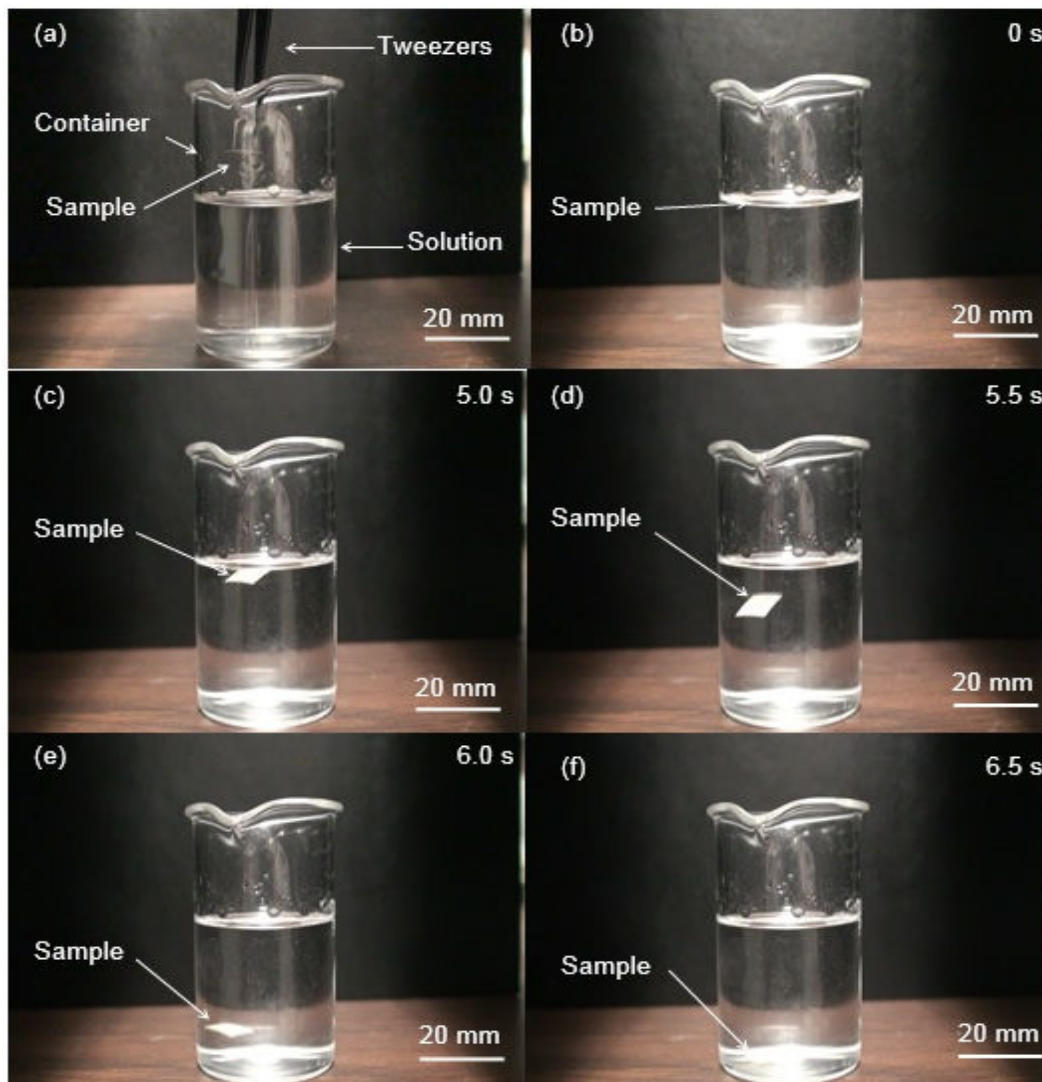
Figure 5-3: Side view of the sinking process of a sample in the liquid with 50% IPA and 50% water. The top surface of the sample is structured with ZnO nanowire-covered SU-8 square micropillars. (a) The sample is put on the liquid surface using a pair of tweezers. (b) The liquid spreads on the top surface of the sample, while the sample still floats on the liquid surface. (c) The sample starts to sink after the spreading is complete. (d, e) It is sinking. (f) The sample finally rests on the bottom of the container.
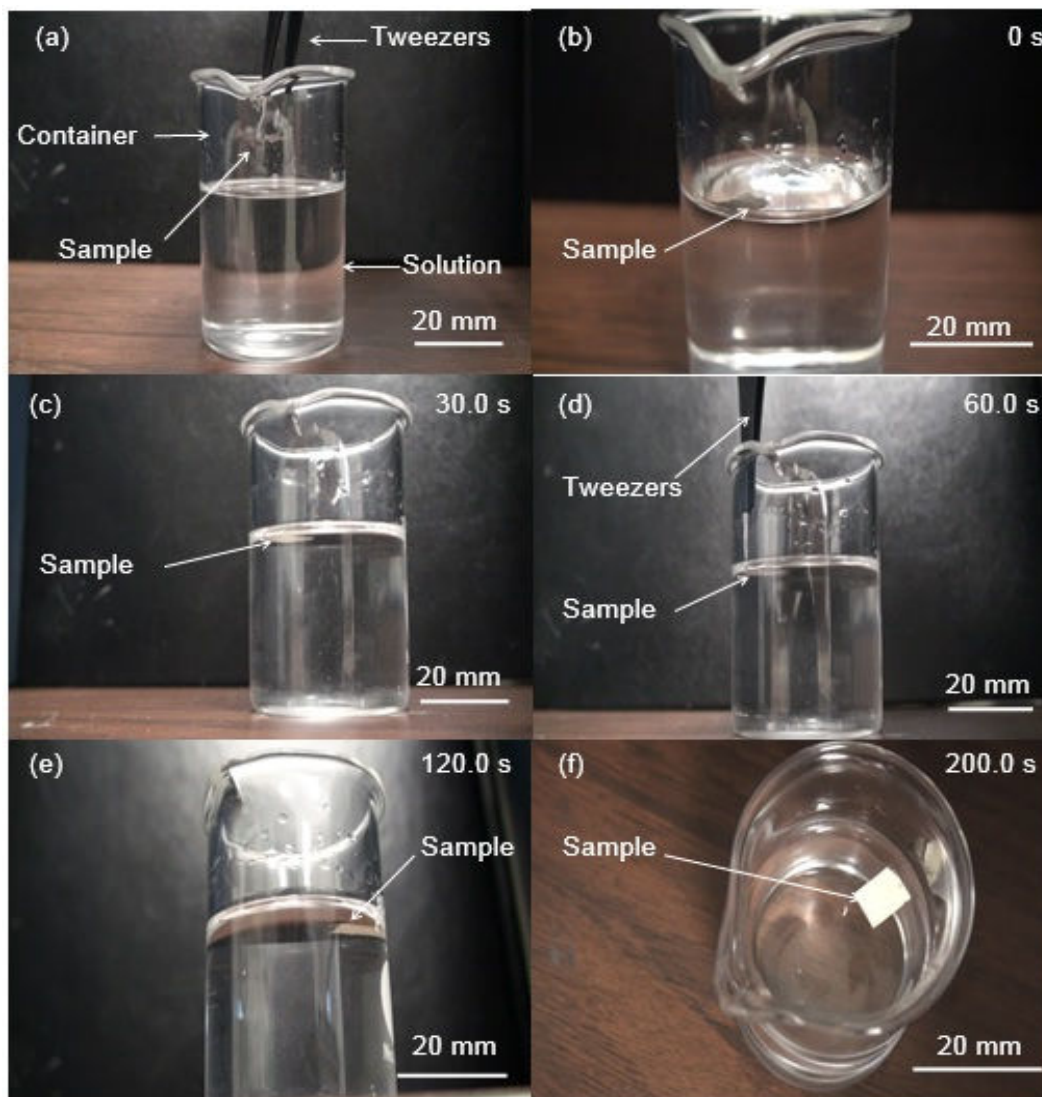
Figure 5-4: Side view of the sample shown in Fig. 10 on the surface of the liquid with 50% IPA and 50% water. The sample is flipped over with the originally bottom surface facing up now. (a) The sample is put on the liquid surface using a pair of tweezers. (b, c) The sample floats on the liquid surface. (d) The sample does not sink after it has been slightly pressed down by tweezers. (e, f) The sample still floats on the liquid surface.

Chapter 6

Conclusions

Creation of superwetting surfaces using roughness structures is explored in this work. Modulating roughness structures and surface texture can dramatically alter the apparent contact angle. As demonstrated in this work, it is important to have a small value of $f$ to create superwetting surfaces having nearly $0^o$ contact angle when the intrinsic contact angle is relatively large, say for instance 40° or above. After series of experiments it was found that the sample with nanostructures covered microstructures is the one which meets this requirement. A total of five samples were designed, fabricated and tested to validate the theoretical predictions. Through in-situ observation, we gained a detailed understanding of how the Wenzel and Cassie impregnating states were formed in between the roughness structures. Furthermore, we have showed that the created superwetting surface can be used to eliminate the effect of surface tension and sink a floating small plate to the liquid bottom. When the plate having the superwetting structures facing up was kept on the liquid, it sank to the liquid bottom. On the other hand, when the plate was flipped upside down, with the untreated side facing up, it did not sink as the effect of surface tension was not eliminated. The results and insight obtained from this research work may also be applied for other applications such as micro submarine, microfluidic devices like microlenses and droplet based lab on a chip and polymeric bio implants.

References

(1) Hu, D. L.; Chan, B.; Bush, J. W. M. The hydrodynamics of water strider locomotion. *Nature* **2003**, *424*, 663-666.

(2) Hu, D. L.; Bush, J. W. M. Meniscus-climbing insects. *Nature* **2005**, *437*,733-736.

(3) Song, Y. S.; Suhr, S. H.; Sitti, M. Modeling of the supporting legs for designing biomimetic water strider robots. *Proceedings of the International Conference on Robotics and Automation* **2006**, Orlando, FL, pp. 2303-2310.

(4) Luo, C.; Li, H.; Liu, X. Propulsion of microboats using isopropyl alcohol as a propellant. *Journal of Micromechanics and Microengineering* **2008**, *18*, 067002.

(5) Luo, C.; Qiao, L.; Li, H. Dramatic Squat and Trim Phenomena of MM-Scaled SU-8 Boats Induced by Marangoni Effect. *Microfluidics and Nanofluidics* **2010**, *9*, 573-577.

(6) Qiao, L.; Xiao, D.; Lu, F. K.; Luo, C.Control of the radial motion of a self-propelled microboat through a side rudder.*Sensors and Actuators A* **2012**, *188*, 359-366.

(7) Osada, Y.; Gong, J. P.; Uchida, M.; Isogai, N. Spontaneous motion of amphoteric polymer gels on water.*JapaneseJournal of Applied Physics* **1995**,*34*, L511-L512.

(8) Li, H.; Luo, C. Development of a Self-propelled Water Microflotilla.*Microsystem Technologies* **2011**, *17*, 777-786.

(9) Liu, X.; Li, H.; Qiao, L.; Luo, C. Driving mechanisms of cm-scaled PDMS boats of respective close and open reservoirs.*Microsystem Technologies* **2011**, *17*, 875-889.

(10) Neinhuis, C.; Barthlott, W. Characterization and distribution of water-repellent, self-cleaning plant surfaces. *Ann. Bot.***1997**, *79*, 667-677.

(11) Xiang, M.; Wilhelm, A.; Luo, C. Existence and Role of Large Micropillars on the Leaf Surfaces of The President Lotus. *Langmuir* **2013**, *29*, 7715−7725.

(12)  Qiao, L.; Xiang, M.; Luo, C. Increase Buoyancy of a Small plate Using Micropillar*s.*
*Sensors and Actuators A* **2012**,*182*, 136-145.

(13)  McHale, G.; Shirtcliffe, N. J.; Aqil, S.; Perry, C. C.; Newton, M. I. Topography Driven
Spreading. *Phys. Rev. Lett*. **2004**, *93*, 036102.

(14)  Extrand, C. W.; Moon, S. I.; Hall, P.; Schmidt, D. Superwetting of Structured
Surfaces. *Langmuir* **2007**, *23*, 8882-8890.

(15) Wenzel, R. N. Resistance of solid surfaces to wetting by water.*Industrial &
Engineering Chemistry* **1936**,*28*, 988-994

(16) Cassie A. B. D.; Baxter S. Wettability of porous surfaces. *Trans. Faraday Soc.***1944,**
*40*, 546-551.

(17) Bico, J.; Thiele, U.; Quéré, D. Wetting of Textured Surfaces.*Colloids Surf., A* **2002**,
*206*, 41-46

(18) Bormashenko, E.; Pogreb, R.; Stein, T.; Whyman, G.; Erlich, M.; Musin, A.;
Machavariani, V.; Aurbach, D. Characterization of RoughSurfaces with Vibrated
Drops. *Phys. Chem. Chem. Phys* **2008**, *10*, 4056-4061.

(19) Luo, C. Maximum loading capacities of solid fragments with pores and rough
surfaces. *Nano Bulletin* **2012**, Vol. *1* (1), 120106.

(20)  Concus, P.; Finn, R. Discontinuous behavior of liquids between parallel and tilted
plates. *Phys. Fluids* **1998,** *10,* 39-43.

(21) Belinkov, M. K.; Marmur, A.; Trabold, T.; Dadheech, G. V. Groovy Drop: Effect of
Groove Curvature on Spontaneous Capillary Flow. *Langmuir* **2007,** *23,* 8406-8410.

(22) Feng, J.; Rothstein, J. P. One-way wicking in open micro-channels controlled by
channel topography. *Journal of Colloid and Interface Science* **2013**, *404*, 169-178.

(23) Atthi N.; Nimittrakoolchai O. U.; Supothina S.; Supadech J.; Jeamsaksiri W.;
Pankiew A.; Hruanun C.; Poyai A. An effect of silicon Micro/Nano-patterning Arrays

on Superhydrophpboc surfaces. *Journal of Nanoscience and Nanotechnology* **2011,** *11,* 1-7.

(24)  Roach P,; Shirtcliffe  N. J.; Newton M. I. Progress in superhydrophobic surface development. *Soft Matter* **2008**, *4*, 224-240.

(25)  Li X. M.; Reinhoudt D.; Calama M. C. What do we need for a superhydrophobic surface? A review on the recent progress in the preparation of superhydrophobic surfaces. *Chem. Soc. Rev.* **2007,** *36*, 1350-1368.

(26) Lorenz H.; Despont M.; Renaud P. Fabrication of photoplastic high-aspect ratio micro parts and micromolds using SU-8 UV resist. *Microsystem Technologies* **1998**, *4*, 143-146.

(27) Madou, M. *Fundamentals of Microfabrication* **1995,** CRC Press: Boca Raton, FL.

(28) Wang, B. G.; Shi, E. W.; Zhong, W. Z. Understanding andcontrolling the morphology of ZnO crystallites under hydrothermal conditions. *Cryst. Res. Technol*. **1997**, *32*, 659-667.

Biographical Information

Varun Garg has received a Bachelor's of Engineering Degree in Mechanical Engineering from Vishwakarma Institute of Technology (V.I.T), Pune University, India in July 2012. During his undergraduate studies, his senior year project was "Analysis and characterization of low speed high lift airfoil using subsonic wind tunnel" and assisted a project on metal matrix composites, in which he fabricated a set up that can help increase the tensile strength of the alloy, by effectively dispersing the SiC particles, the alloy was specifically designed for mechanical or aerospace applications. He was the founder member of various organizations on campus and worked with fellow students to discover new projects and interesting challenges. He was the leader for the team that represented V.I.T at SAE Aero Design West 2011, Texas USA, organized by Lockheed Martin, the team received three awards, including the best overall performance. He also worked on a start- up company called Airkraft as the founder and director for a year and a half. During this time he organized 20 plus workshops for 350 plus engineering students.

He has been a Graduate student in the Mechanical & Aerospace Engineering Department at UTA since August 2012. He joined Dr.Cheng Luo's group in October 2012 and worked with his group on design and fabrication of micro submarines and development of superwetting surfaces to eliminate surface tension effect. His interests are majorly project management, micro/electro mechanical systems and mechanical designing.